Analysis of the Sapphire Fiber Fabry-Perot Interferometer Fringe Visibility under Different Excitation Conditions

Jiawei ZHANG[1,2], Rui TANG[3*], Dongsheng ZHANG[1,2*] and Minghong YANG[1,2]

[1]*School of Information Engineering, Wuhan University of Technology, Wuhan 430070, China*

[2]*National Engineering Research Center of Fiber Optic Sensing Technology and Networks, Wuhan University of Technology, Wuhan 430070, China*

[3]*AECC Shenyang Engine Institute, Shenyang 110015, China*

[*]Corresponding author: Rui TANG and Dongsheng ZHANG E-mails: dril_don@163.com and 1929673933@qq.com

Abstract: In this paper, a theoretical analysis of how the excitation conditions affect the sapphire fiber Fabry-Perot interferometer (SFPI) visibility was performed. The conditions were considered, in which an SFPI was excited by a single-mode fiber (SMF), a multimode fiber (MMF), and a fiber collimator. The finite difference method (FDM) was used to realize the numerical solution of the modal electric fields, and then, the modal excited distributions in the sapphire fiber and the SFPI visibility were calculated. The results showed that different numbers of modes were excited in sapphire fibers under different excitation conditions and finally affected the fringe visibility of the SFPI. The fiber collimator excited the fewest modes and the visibility remained at the highest level. Finally, an experiment was performed, and the experimental results agreed well with the theoretical results.

Keywords: Optical fiber sensing; sapphire fiber; Fabry-Perot interferometer; visibility; numerical solution

Citation: Jiawei ZHANG, Rui TANG, Dongsheng ZHANG, and Minghong YANG, "Analysis of the Sapphire Fiber Fabry-Perot Interferometer Fringe Visibility under Different Excitation Conditions," *Photonic Sensors*, 2024, 14(3): 240305.

1. Introduction

Fiber sensors have attracted much attention in recent years due to advantages, such as the small size, light weight, immunity to electromagnetic interference, and ease of embedding. Regular silica fiber sensors cannot be used in environments over 1 000 ℃ because they will be soft. To meet the demand of sensing under ultrahigh temperature circumstances, sapphire fibers, whose melting point is 2 050 ℃, have shown great prospects. To avoid the effect of birefringence, the sapphire fibers used for sensing are usually *c*-axis sapphire fibers, the profiles of which are hexagons. The diameters of the circumcircles of the hexagonal sapphire fibers are usually 50 μm to 200 μm without a cladding layer. Many researchers are studying the addition of a cladding layer to sapphire fibers [1–4]. However, the mismatch in the thermal expansion coefficient between the core and cladding layer brings significant challenges, preventing the widespread application at present. The non-cladding structure makes the refractive index (RI) difference between the core layer (the RI of sapphire is 1.762) and cladding layer (the RI of air is approximately 1) very large and further results in a large transmission loss

Received: 31 May 2023 / Revised: 25 September 2023

DOI: 10.1007/s13320-024-0700-x
Article type: Regular

and a large number of modes, which brings issues for phase demodulation sensing systems, such as Fabry-Perot (FP) sensing systems.

A sapphire fiber FP sensing system consists of a sapphire fiber FP interferometer (SFPI), a transmitting fiber, and a source/signal processing system. Because of the large transmission loss, the length of the sapphire fiber used in the sensing system should be short. Therefore, sapphire fibers are only used in high-temperature areas, and a silica fiber is coupled with the SFPI to transmit light signals between the source/signal processing system and the SFPI. Each mode in the SFPI forms a sine-like function spectrum. The spectra generated by different modes have different periods, and the superposition of these spectra generates a new sine-like function but with the low visibility. As the number of modes is relatively large in sapphire fibers, the visibility of the SFPI spectrum is relatively low.

One of the methods to improve the visibility is to increase the parallelism of the FP end face. J. Wang *et al*. [5] improved the polishing technique and fabricated multiplexed sapphire FP sensors for temperature sensing. Y. Zhu *et al*. [6, 7] used sapphire wafers, the two faces of which were highly parallel, to fabricate FP temperature sensors. This structure was also later used for pressure sensing [8–10]. The other method is to decrease the number of modes in the sapphire fiber. Y. Cheng *et al*. [11, 12] offered a windmill-structure fiber design to filter high-order modes. C. Hill *et al*. [13, 14] used a wet etching method to successfully fabricate single-mode sapphire fibers. X. Feng *et al*. [15] filtered the high-order modes in an SFPI by using a multistage fiber, which was fabricated by fusing silica fibers with different core diameters. J. Zhang *et al*. [16] presented a high-visibility sapphire FP sensing system by using a fiber collimator to control the divergence angle of the light, before it was injected into the SFPI.

Compared with the parallelism-improvement method, the method of reducing the number of modes is more effective in improving the SFPI visibility. It is necessary to perform theoretical analyses to summarize the above regularity and provide directions for further research. F. Pérennès *et al*. [17] built a model of low-finesse FP sensors illuminated by a multimode optical fiber based on the geometrical optics knowledge. They deduced the equation of the visibility and researched how the cavity length, tilt, and wedge affected the FP interferometer (FPI) visibility. M. Han *et al*. [18, 19] presented a model of low-finesse multimode fiber FP interferometers based on wave optics. In addition to the cavity length and wedge, their model also included how the mode power distribution affects the visibility. W. Dai *et al*. [20] investigated the effect of light source injection conditions on the field distribution of polymer multimode fibers (MMFs) with the beam propagation method. With the simulated distribution, they realized the relationship between the modal power and the offset length, and finally explained how the offset launch technology reduces the differential modal delay. F. Mumtaz *et al*. [21] demonstrated the number of strongly guided modes propagating in sapphire fibers by solving the modal equation with a numerical solution method. The eigenmode values were obtained by using a numerical root finder. With the eigenmode values, the confinement loss parameter and dispersion parameter were also calculated.

In this paper, theoretical research on how different excitation conditions affect the hexagonal-profile SFPI visibility is performed. Three different excitation conditions, in which the SFPI is excited by a single-mode fiber (SMF), an MMF, and a fiber collimator, are studied. In Section 2, a theoretical analysis is performed on the excitation conditions caused by different transmitting fibers. In Section 3, the SFPI fringe

visibility under different excitation conditions are calculated. Section 4 presents an experiment to verify the theoretical analysis.

2. Analysis of modal excitation conditions

2.1 Theory

Figure 1 shows a schematic of a typical SFPI. The light from the transmitting fiber is coupled into the sapphire fiber and excites different modes $\mathbf{E}_k$ ($k=1, 2, \cdots, N$). Two sapphire fibers, which are placed against each other with parallel end faces R_1 and R_2, form the FP cavity. The light reflected from end faces R_1 and R_2 interferes and forms a sine-like function spectrum whose period is related to the cavity length. For the convenience of analysis, the sapphire fiber is assumed to be a regular waveguide, which means that the modes transmitting in the fiber are orthogonal, and the coupling phenomenon will not occur between the modes with different mode orders.

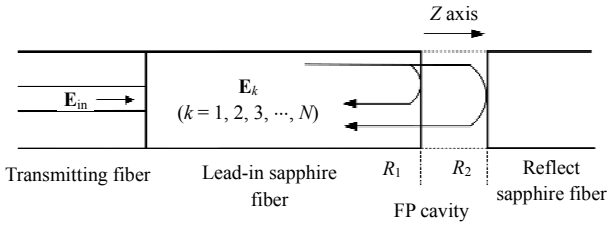

Fig. 1 Schematic of a sapphire FP interferometer.

With different transmitting fibers, the electric field coupled into the sapphire fiber is different, and then, the excitation level of each mode is different. The optical path differences (OPDs) between different modes are the main factors that influence the SFPI visibility, so the different modal excited distributions will influence the SFPI spectrum visibility.

The total number of modes in a sapphire fiber can be approximately calculated by [22]

$$N \approx \frac{4}{\pi^2}\left(\frac{2\pi}{\lambda_0}\cdot\frac{a}{2}\cdot\sqrt{n_1^2-n_2^2}\right)^2 = 54\,751. \tag{1}$$

In the equation, $\lambda_0=1.55$ μm; $a=125$ μm, which is the diameter of the sapphire fiber; $n_1=1.762$, which is the RI of the sapphire fiber; $n_2=1$, which is the RI of the air cladding.

In practice, not all the modes can be excited. The excitation level of the kth mode in the sapphire fiber can be described by the coupling efficiency between the mode and the input field, calculated by (2)

$$p_k^2 = \frac{\left(\iint_R \mathbf{E}_{in}\cdot\mathbf{E}_k \mathrm{d}x\mathrm{d}y\right)^2}{\iint_R \mathbf{E}_{in}^2 \mathrm{d}x\mathrm{d}y \cdot \iint_R \mathbf{E}_k^2 \mathrm{d}x\mathrm{d}y} \tag{2}$$

where $\mathbf{E}_{in}$ is the output electric field of the transmitting fiber, $\mathbf{E}_k$ is the electric field of different modes in the sapphire fiber, and R is the cross section of the sapphire fiber. For the convenience of analysis, the electric fields $\mathbf{E}_k$ are normalized by (3)

$$\iint_R |\mathbf{E}_k|^2 \mathrm{d}x\mathrm{d}y = 1. \tag{3}$$

The excitation levels of all the modes in the sapphire fiber form the modal excited distribution. From (2), it can be seen that to calculate the modal excited distribution, the electric fields of the transmitting fiber and the electric field of each mode in the sapphire fiber need to be calculated first.

2.2 Numerical solution of electric fields in the sapphire fiber

Figure 2 shows the cross section of the sapphire fiber we analyzed. The diameter of the sapphire fiber is 125 μm with a hexagonal profile. The RI of the sapphire is $n_1=1.762$. Outside of the fiber is the square-profile air cladding layer with an RI of $n_2=1$. The edge length of the air cladding is set as 175 μm. As the electric field we are calculating is a steady field, the Maxwell equation can be changed into the Helmholtz equation [23]. In the core layer, the Helmholtz equation can be expressed as

$$\left(\frac{\partial^2}{\partial x^2}+\frac{\partial^2}{\partial y^2}\right)\mathbf{E}_{core} + \left(n_1^2k_0^2-\beta^2\right)\mathbf{E}_{core} = 0 \tag{4}$$

and in the cladding layer

$$\left(\frac{\partial^2}{\partial x^2}+\frac{\partial^2}{\partial y^2}\right)\mathbf{E}_{cladding} + \left(n_2^2k_0^2-\beta^2\right)\mathbf{E}_{cladding} = 0 \tag{5}$$

where $\mathbf{E}_{core}$ is the electric field in the core layer,

$\mathbf{E}_{\text{cladding}}$ is the electric field in the cladding layer, n_1 is the RI of the core layer, n_2 is the RI of the cladding layer, β is the propagation constant, and $k_0=2\pi/\lambda$. There is an interface condition:

$$\mathbf{E}_{\text{core}} = \mathbf{E}_{\text{cladding}} . \tag{6}$$

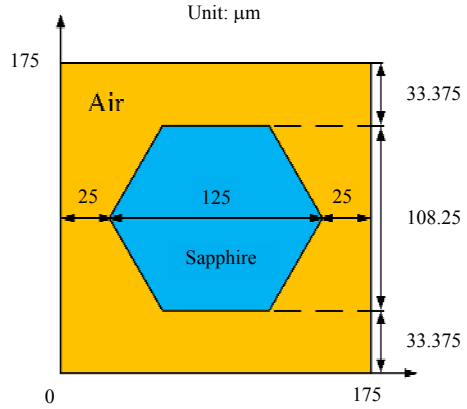

Fig. 2 Geometry parameters of the sapphire fiber.

Only light that satisfies the total-reflection condition can be transmitted in the fiber. Evanescent field theory shows that when total reflection occurs, the light will penetrate into the optically thinner medium [22]. The order of the magnitude of the penetration length will be the same as that of the light wavelength. As the light wavelength in our analysis is 1.55 μm, it can be assumed that the air cladding layer we set is large enough such that the light cannot be transmitted to the air layer boundary. And then, the boundary condition can be written as

$$\mathbf{E}_{\Omega} = 0 \tag{7}$$

where Ω is the boundary of the square air cladding layer.

As the sapphire fiber is a hexagonal-profile light waveguide, the proper method is to use a numerical solution, transforming the differential equation into a difference equation and solving it. The finite difference method (FDM) is used to solve the equation. First, the solution area should be discretized. In this work, a square mesh can satisfy the calculation. The mesh size should be smaller than the wavelength of the light, and considering the computation speed, it should not be too small. Therefore, the edge lengths of each element are set as $h_x=h_y=h=0.5$ μm, which is smaller than 1/3 of the wavelength of the light, and the whole area is divided into 350×350 elements. Second, the differential equation is transformed into a difference equation by the five-point method, which is stable on the Dirichlet boundary for elliptic problems [24]. The electric field intensity at each mesh point is recorded as an array: $\mathbf{E}_k=(E_{1,1}, E_{2,1}, E_{3,1}, \cdots, E_{M-1,1}, E_{1,2}, E_{2,2}, \cdots, E_{M-1,N-1})^{\mathrm{T}}$, with $M=N=350$. The differential term at each mesh point can be approximated by the difference term:

$$\left.\frac{\partial^2 \mathbf{E}_k}{\partial x^2}\right|_{\substack{x=i\\y=j}} = \frac{E_{i-1,j}-2E_{i,j}+E_{i+1,j}}{h^2} \tag{8}$$

$$\left.\frac{\partial^2 \mathbf{E}_k}{\partial y^2}\right|_{\substack{x=i\\y=j}} = \frac{E_{i,j-1}-2E_{i,j}+E_{i,j+1}}{h^2} . \tag{9}$$

Therefore, for a mode with the propagation constant β_k, the equation at any mesh point is

$$\frac{E_{i-1,j}-2E_{i,j}+E_{i+1,j}}{h^2}+\frac{E_{i,j-1}-2E_{i,j}+E_{i,j+1}}{h^2}+(\mathbf{C}_l-\beta_k^{\,2})E_{i,j}=0 \tag{10}$$

where $\mathbf{C}_l = n_l^2 k_0^2$, $l=1$ for the core layer, $l=2$ for the cladding layer, and β_k is the propagation constant of the kth mode.

Equation (10) can be presented as the following matrix equation:

$$\frac{1}{h^2}(\mathbf{d}_{x,x}+\mathbf{d}_{y,y})\mathbf{E}_k+(\mathbf{C}_l-\beta_k^2)\mathbf{E}_k = 0+\mathbf{E}_{\Omega} . \tag{11}$$

In the equation, $\mathbf{E}_k=(E_{1,1}, E_{2,1}, E_{3,1}, \cdots, E_{M-1,1}, E_{1,2}, E_{2,2}, \cdots, E_{M-1,N-1})^{\mathrm{T}}$. And the parameters $\mathbf{d}_{x,x}$, $\mathbf{d}_{y,y}$, and $\mathbf{C}_l$ are carefully introduced in the Appendix.

Equation (11) can be transformed into an eigenvalue equation by combining it with (12)

$$\frac{1}{h^2}(\mathbf{d}_{x,x}+\mathbf{d}_{y,y}+\mathbf{C}_l)\mathbf{E}_k = \beta_k^{\,2}\mathbf{E}_k . \tag{12}$$

By solving (12), a series solution of the eigenvalue β_k and eigenvector $\mathbf{E}_k$ can be calculated. Each β_k is the propagation constant of a guide mode in the sapphire fiber. The electric field of each mode can be demonstrated by the restoring eigenvector $\mathbf{E}_k$ into a 349×349 matrix and adding the boundary condition in (7). The mode electric field is then

normalized by (3). Figure 3 shows the fields of several typical modes calculated by MATLAB.

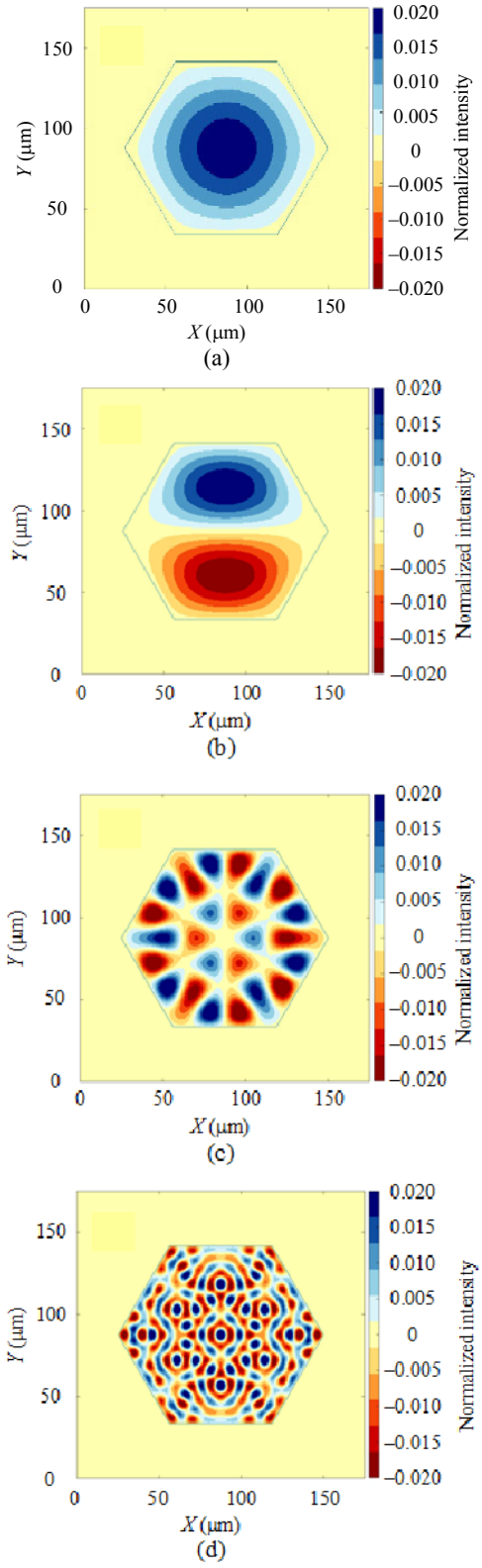

Fig. 3 Electric field of different modes in the sapphire fiber: (a) $k=1$, (b) $k=2$, (c) $k=40$, and (d) $k=299$.

As mentioned before, the air cladding layer should be large enough to satisfy the boundary condition in (7). Figure 4 shows the electric field intensity along the diagonal line $Y=72.5$ μm. The coordinates of the fiber boundary are $X=25$ μm and $X=150$ μm. The electric field intensity decreases to zero at the boundary. This result proves that the setting of the size of the air cladding is reasonable. As the curve is convergent and smooth, the setting of the mesh size is reasonable.

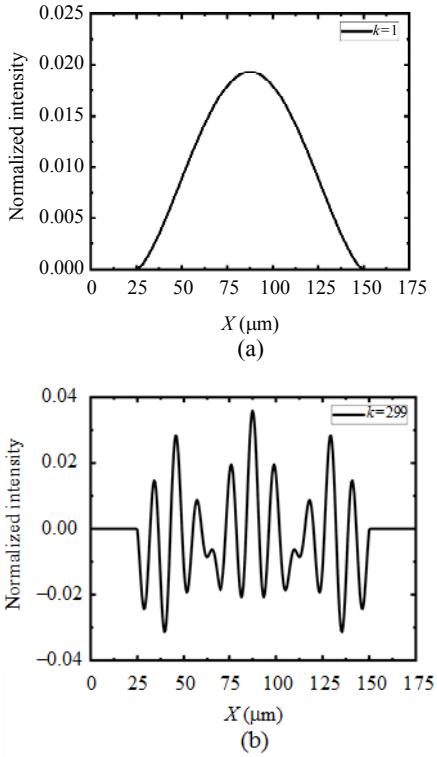

Fig. 4 Electric field intensity distributions of different modes along the diagonal line: (a) $k=1$ and (b) $k=299$.

2.3 Emitted electric field of an SMF and an MMF

With the same method, the emitted electric fields of an SMF and an MMF are calculated. The core diameters of the SMF and MMF are 9 μm and 105 μm, respectively. It should be mentioned that the emitted field of the MMF is the summation of the electric fields of all the modes in the fiber. As the MMF is long and curved in practical use, the modes can be assumed to be uniformly excited, that is, $p_{MK}=1/N_{MMF}$. The results are shown in Fig. 5.

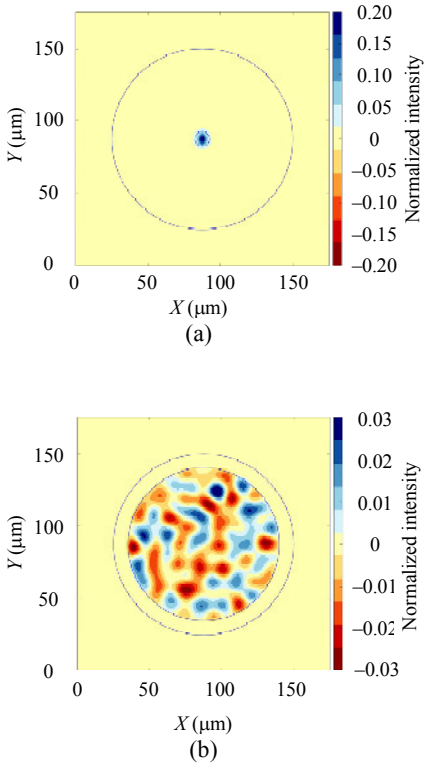

Fig. 5 Emitted electric field: (a) SMF and (b) MMF.

2.4 Emitted electric field of the fiber collimator

A schematic of the collimator-based SFPI is shown in Fig. 6. A fiber collimator, which replaces the MMF, is used as the transmitting fiber. The fiber collimator is made by fusing a section of a graded-index fiber (GIF) with an SMF [16]. The length of the GIF is a quarter of its self-imaging period, so the GIF can work as a collimator. With the help of the collimator, the visibility of this system is significantly improved.

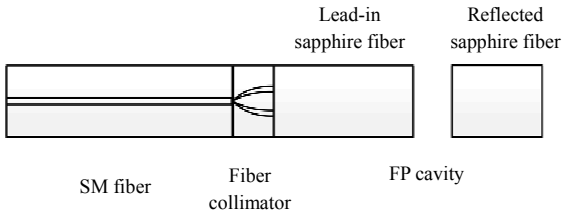

Fig. 6 Schematic of the collimator-based sapphire fiber FP sensing system.

The simulation is performed with the RSOFT software to calculate the emitted electric field of the collimator. The simulation model is set as shown in Fig. 7(a). The GIF with a diameter of 62.5 μm is coupled with an SMF with a diameter of 9 μm. Because the length of the SMF does not affect the light transmission in the GIF, the length of the SMF is set to be short to increase the simulation speed, with a value of 50 μm. The RI of the GIF is set as (13), and the self-imaging period of the GIF can be calculated, which is 816 μm. Therefore, the length of the GIF used as a collimator is 204 μm. Figure 7(b) shows the simulation result. The electric field is mainly focused in a circle with a diameter of 40 μm:

$$n(r)=\begin{cases} n_1\cdot\sqrt{1-2\Delta\left(\dfrac{r}{31.25\ \mu\text{m}}\right)^2} & (0\le r\le 31.25\ \mu\text{m}) \\ n_2 & (r>31.25\ \mu\text{m}) \end{cases} \quad (13a)$$

$$\Delta=\frac{n_1-n_2}{n_1}=\frac{1.46-1.42}{1.46}=0.028 \quad (13b)$$

where n is the RI, r is the distance between the point and the center of the fiber, n_1=1.46 is the RI of the core layer, n_2=1.42 is the RI of the cladding layer, and Δ is the relative difference between n_1 and n_2.

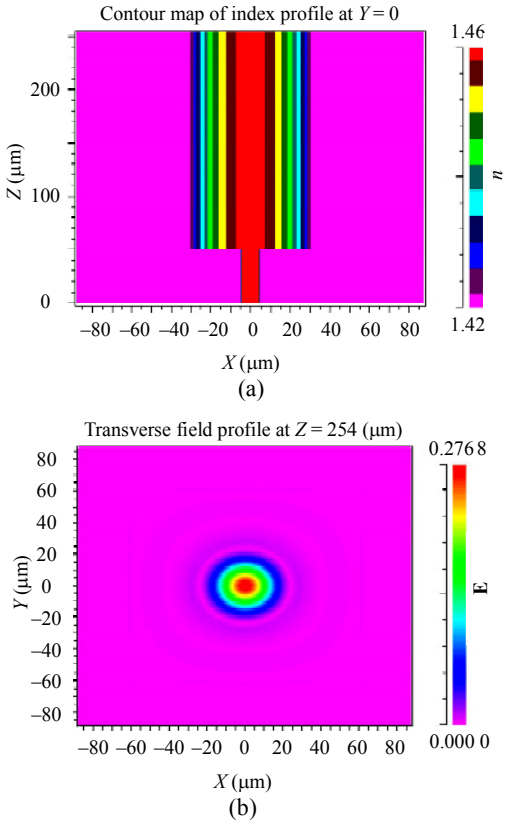

Fig. 7 Simulation model and the result: (a) model set in the simulation and (b) simulation result of the emitted electric field of the fiber collimator.

2.5 Results and analyses

With the electric fields, the modal excited distribution can be calculated with (2). We calculated the coupling efficiency of the first 400 modes in the sapphire fiber. The values of the summation of all 400 mode coupling efficiencies for the three excitation conditions were 0.9713, 0.9990, and 0.9997, which mean that modes whose orders are higher than k=400 can be neglected when performing the analyses. The result is shown in Fig. 8.

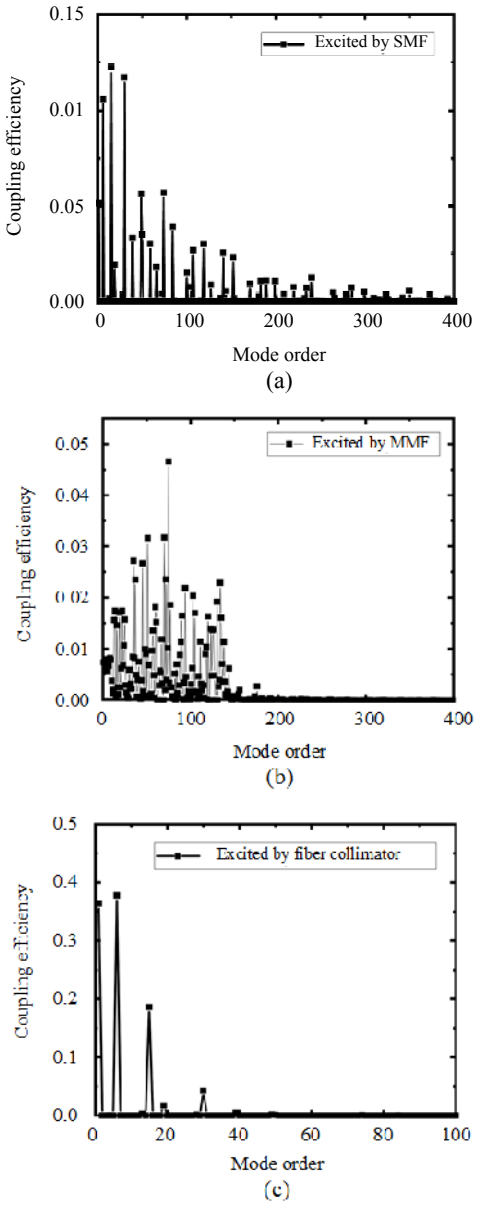

Fig. 8 Modal excited distributions of the sapphire fiber under different excitation conditions: (a) SMF excitation, (b) MMF excitation, and (c) fiber collimator excitation.

The maximum coupling efficiency values in the three conditions are 0.122, 0.047, and 0.378. It is assumed that the modes whose coupling efficiency is less than 1% of the maximum value can be identified as not excited. Then, the numbers of excited modes under the three conditions can be counted, which are 46, 128, and 6.

It can be seen that when being excited by an MMF, the number of excited modes is the largest, and the excited modes are mainly distributed in the first 200 modes. When being excited by an SMF, the number of excited modes is fewer, and the modes are dispersed among all the modal orders. Finally, with the help of the fiber collimator, the number of excited modes in the sapphire fiber is dramatically reduced to 6. The power is mainly focused on the three modes whose mode order is k=1, 6, and 15.

Figure 9 shows the electric field of these three modes along with the emitted field of the collimator. The 6th mode in the sapphire fiber best matches the collimator, so it has the largest coupling efficiency value.

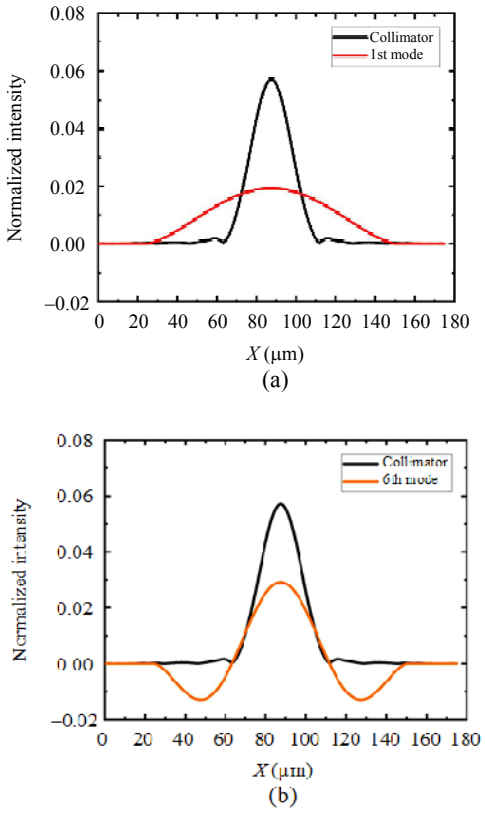

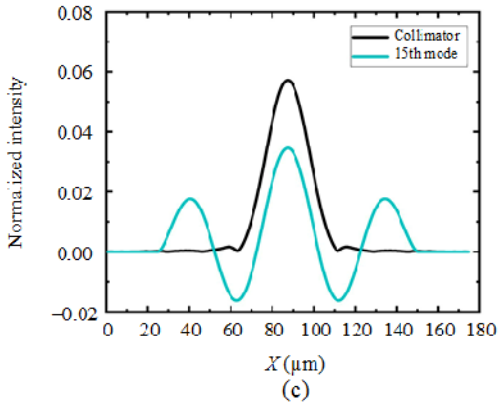

Fig. 9 Electric field of the fiber collimator and the main excited modes in the sapphire fiber: (a) 1st mode, (b) 6th mode, and (c) 15th mode.

3. Visibility

With the modal excited distribution p_k and the electric fields in the sapphire fiber $\mathbf{E}_k$, the total electric fields in the sapphire fiber can be expressed as

$$\begin{aligned}\mathbf{E}_{\text{total}} &= \sum_{k=1}^{N} p_k \mathbf{E}_k \exp(-\mathrm{j}\beta_k z) \\ &= \sum_{k=1}^{N} p_k \psi_k \exp(-\mathrm{j}\beta_k z)\cdot \mathbf{e}_k \end{aligned} \tag{14}$$

where ψ_k is the absolute value of the intensity of each point in electric fields $\mathbf{E}_k$, $\mathbf{e}_k$ is a unit vector representing the polarization of the mode.

As the electric fields $\mathbf{E}_k$ are orthogonal and normalized, the intensity of the light can be expressed as

$$\begin{aligned} I &= \left\langle \mathbf{E}_{\text{total}} \cdot \mathbf{E}_{\text{total}}^{*} \right\rangle \\ &= \sum_{k=1}^{N} (p_k \psi_k)(p_k \psi_k)^{*} \left\langle \mathbf{e_k} \cdot \mathbf{e_k}^{*} \right\rangle \\ &= \sum_{k=1}^{N} |p_k|^2 . \end{aligned} \tag{15}$$

The sapphire fiber FPI visibility can be expressed as [18]

$$\begin{aligned} V_b &= \frac{|I_{\max} - I_{\min}|}{|I_{\max} + I_{\min}|} \\ &= \frac{\left| 2\sum_{k=1}^{N} |p_k|^2 |\eta_k| \cos(\nabla\varphi_{01} + \varphi_k) \right|}{\left| \sum_{k=1}^{N} |p_k|^2 + \sum_{k=1}^{N} |p_k|^2 (|\eta_k|^2 + c_k^2) \right|} . \end{aligned} \tag{16}$$

In the equation,

$$\eta_k = \frac{\left(\iint_R \mathbf{E}_k \cdot \mathbf{E}_k' \mathrm{d}x\mathrm{d}y \right)^2}{\iint_R \mathbf{E}_k^2 \mathrm{d}x\mathrm{d}y \cdot \iint_R (\mathbf{E}_k')^2 \mathrm{d}x\mathrm{d}y} \tag{17}$$

$$\mathbf{E}_k'(x,y) = F_{x,y}^{-1}\{F_{x,y}[\mathbf{E}_k(x,y)]H(f_x, f_y; z)\} \tag{18}$$

$$H(f_x, f_y; z) = \exp\{\mathrm{j}k_0 z\sqrt{1 - f_x^2 - f_y^2}\} \tag{19}$$

where f_x and f_y are the spatial frequencies, and $F_{x,y}$ and $F_{x,y}^{-1}$ are the two-dimensional discrete Fourier transform and inverse transform.

Moreover,

$$\sum_{k=1}^{N} |p_k|^2 (|\eta_k|^2 + c_k^2) = \frac{a^2}{(a + 2d\tan\theta_{\max})^2} \tag{20}$$

where d is the cavity length, $\theta_{\max} = \arccos(\beta_{\max}/(n_1 k_0))$ is the maximum divergence angle of the light, $n_1 = 1.762$, $k_0 = 2\pi/\lambda$, $\lambda = 1.55$ μm, and $\beta_{\max}$ is the maximum value of all the propagation constants β_k, which is defined in (12).

The calculation result is shown in Fig. 10. It shows the relationship between the visibility and the FP cavity length when the sapphire fiber FPI is excited by the SMF, MMF, and fiber collimator.

The visibility under the three excitation conditions starts at 100% when the cavity length is zero and decreases as the cavity length increases. When excited by the MMF, the SFPI visibility quickly drops to a minimum value of 1.91% when the cavity length is 270 μm. As the cavity length continues to increase, some sidelobes appear. When excited by the SMF, the visibility decreases to 6.96% as the cavity length increases to 1300 μm. During the whole process, the visibility is higher than that with the MMF. When excited by the fiber collimator, the visibility decreases quite slowly. When the cavity length is 1300 μm, the visibility is still 49.97%. During the whole process, the visibility remains at a high level.

It should be noted that the calculation is based on the assumption that the modes excited in the sapphire fiber are orthogonal. However, in practice, fiber core size variations and fiber bending will

cause mode coupling. Then, more modes will be excited, and the visibility will be lower than the calculation results.

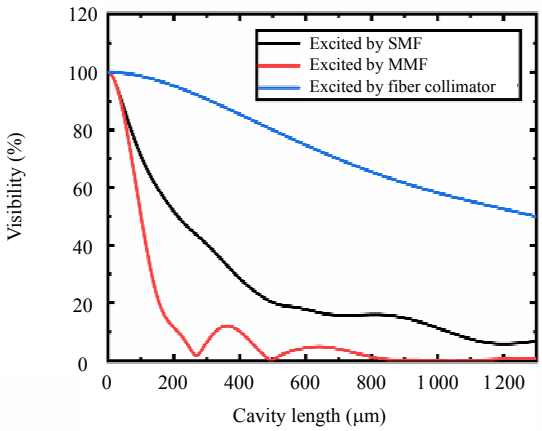

Fig. 10 SFPI visibility under different excitation conditions.

4. Experimental verification

Several experiments were conducted to verify the theoretical analysis. An SFPI was connected to different transmitting fibers, and the visibility variation was tested under different excitation conditions. Here, we take the example of the SMF used as the transmitting fiber to introduce the experimental configuration.

A schematic of the experiments is shown in Fig. 11. A C+L broadband source and an optical spectrum analyzer (OSA) were connected to the input port of an SMF coupler. The output port of the coupler was connected to a sapphire fiber with a diameter of 125 μm with the help of a fiber connector. The sapphire fiber should be sufficiently short to decrease the mode coupling caused by the core size variation. The length of the sapphire fiber in this experiment was 10 cm. The two polished sapphire fibers were set on the five-dimensional microdisplacement stage and formed an FP cavity in a ceramic tube. The spectra were recorded by the OSA.

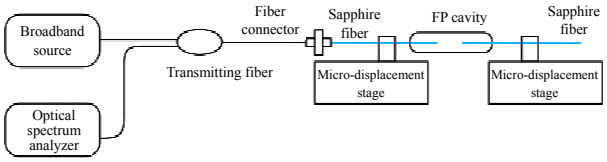

Fig. 11 Experimental configuration.

The FP cavity length was changed from 0 to 1 300 μm by adjusting the microdisplacement stage, and the spectra were recorded during the process. After that, the transmitting fiber was replaced by a 105 μm/125 μm MMF coupler and a fiber collimator to measure the visibility under different excitation conditions. The fiber collimator was made by fusing a quarter-period graded-index fiber with the SM fiber and was packaged as an FC/PC plug [16]. Then, the collimator and the sapphire fiber were connected with the help of a fiber connector, as shown in Fig. 12. The divergence angle was tested to be 5.8°. Spectra were recorded during the experimental process, and the cavity length was calculated based on these spectra.

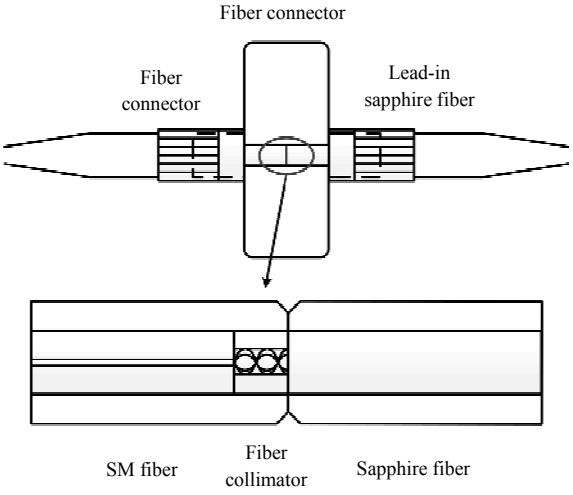

Fig. 12 Details of how the fiber collimator is coupled with the sapphire fiber.

During the experiment, when the SFPI was excited by the MMF, interference fringes were detected only when the cavity length was less than 120 μm. Figure 13 shows the typical spectra. It can be seen that there is much noise in the spectra. Figures 13(a) and 13(b) show the spectra when the SFPI is excited by the MMF and the cavity lengths are set to 50 μm and 120 μm by the microdisplacement stage. According to the calculation based on the spectra, the cavity lengths are 47 μm and 126 μm, which agree with the

theoretical results. Figure 13(c) shows the spectrum when the SFPI is excited by the MMF and the cavity length is set to 220 μm. It can be seen from the spectrum that the interference fringes cannot be distinguished from the background noise, so the cavity length was not calculated.

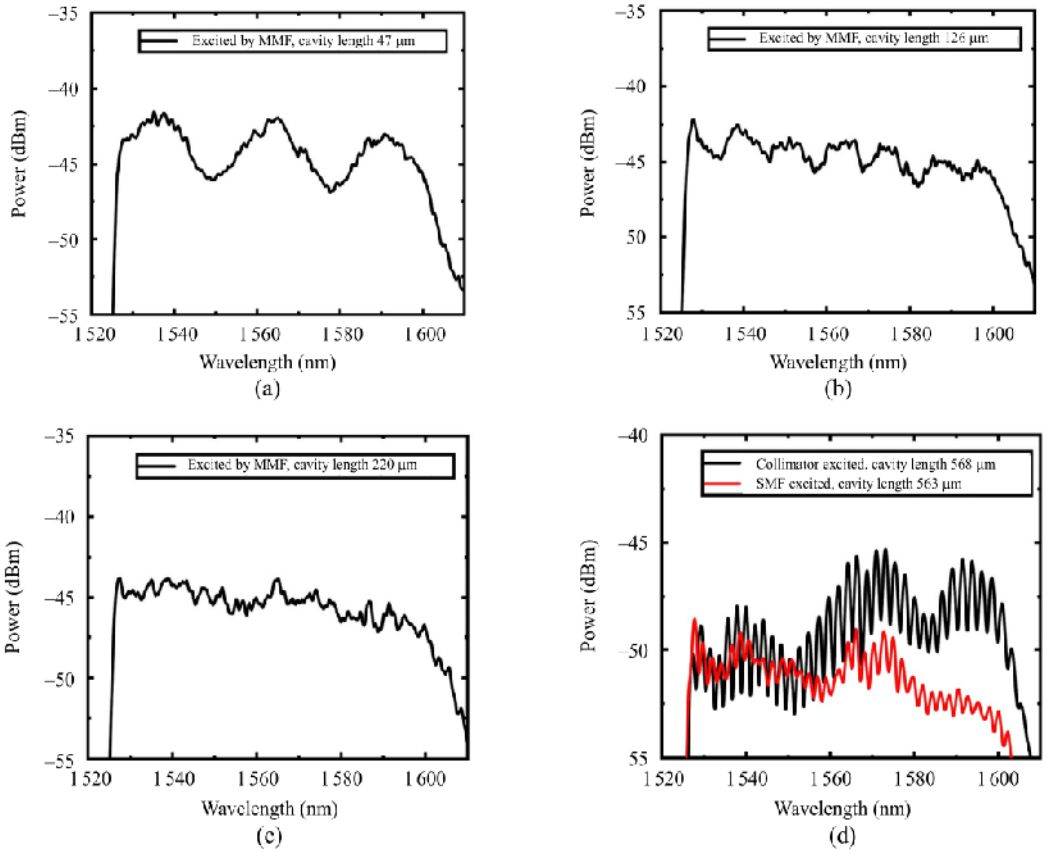

Fig. 13 Spectra of the SFPI when (a) excited by the MMF and the cavity length is set to 50 μm, (b) excited by the MMF and the cavity length is set to 120 μm, (c) excited by the MMF and the cavity length is set to 220 μm, and (d) excited by the SMF and fiber collimator and the cavity length is set to 560 μm.

When the SFPI was excited by the SMF and the collimator, fringes could be detected during the whole process. The visibility when excited by the collimator is larger than that when excited by the SMF. Figure 13(d) shows the contrast spectra of these two excitation conditions. The cavity length is set to 560 μm, and the values obtained from the calculation based on the spectra are 563 μm and 568 μm.

As the cavity length was increased, the spectra at 12 different cavity lengths were recorded. Considering that, in practice, the end faces of the sapphire fiber cannot be strictly parallel with each other, the wedge angle between them will cause a decrease in visibility [17]. Therefore, the theoretical results need to be corrected by multiplying by a constant. Here, the theoretical results were multiplied by 0.56, and the experimental results agree well with the corrected theoretical results, as Fig. 14 shows.

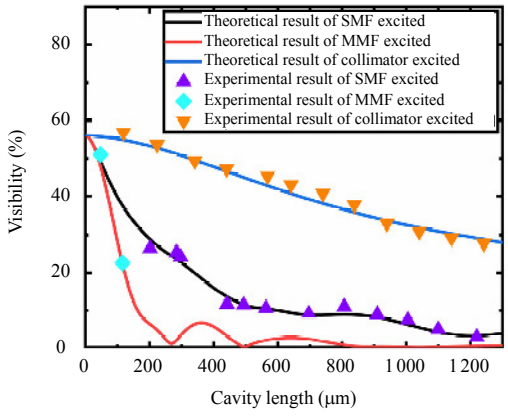

Fig. 14 Comparison between the theoretical results and the experimental results.

5. Conclusions

A theoretical analysis was performed on how excitation conditions affect the SFPI visibility. Three conditions, including SMF, MMF, and fiber collimator excitation conditions, were considered. The modal excited distribution in the sapphire fiber and the SFPI visibility at different cavity lengths were calculated.

The electric fields of the SMF, MMF, fiber collimator, and each mode in the sapphire fiber, were calculated first. The electric fields of the SMF, MMF and sapphire fiber were calculated by using the FDM with the help of MATLAB, while the electric field of the fiber collimator was simulated by the RSOFT software. The modal excited distribution in the sapphire fiber was then calculated with these electric fields. The results show that the numbers of excited modes in the SPF when excited by the SMF, MMF, and fiber collimator are 46, 128, and 6, respectively. The SFPI visibility at different cavity lengths under these three excitation conditions was calculated. The results show that, when excited by the fiber collimator, the visibility remained at a higher level and decreased much slower than that at the other excitation conditions as the cavity length increased. Finally, experiments were performed to verify the theoretical results. The SFPI visibility when excited by the SMF, MMF, and fiber collimator was measured. The experimental results agreed well with the theoretical results.

Our analysis indicates that the number of excited modes in the sapphire fiber varies under different excitation conditions, leading to the different visibility of the SFPI. With the help of a fiber collimator, the number of excited modes in the sapphire fibers can be reduced and the visibility of the SFPI can be increased. This study could provide guidance for designing sapphire/silica fiber coupling devices and SFPIs with high visibility.

Appendix

The parameters in (11):

$$\frac{1}{h^2}(\mathbf{d}_{x,x}+\mathbf{d}_{y,y})\mathbf{E}_k+(\mathbf{C}_l-\beta^2)\mathbf{E}_k=\mathbf{0}+\mathbf{E}_\Omega$$

are

$$\mathbf{E}_k=\left(E_{1,1},E_{2,1},\cdots,E_{M-1,1},E_{1,2},E_{2,2},\cdots,E_{M-1,N-1}\right)^{\mathrm{T}}$$

$$\mathbf{d}_{x,x}=\begin{pmatrix}\mathbf{A}&&\\&\ddots&\\&&\mathbf{A}\end{pmatrix}_{(N-1)}$$

$$\mathbf{A}=\begin{pmatrix}-2&1&&\\1&-2&\ddots&\\&\ddots&\ddots&1\\&&1&-2\end{pmatrix}_{(M-1)}$$

$$\mathbf{d}_{y,y}=\begin{pmatrix}\mathbf{B}&\mathbf{I}&&\\\mathbf{I}&\ddots&\ddots&\\&\ddots&\ddots&\mathbf{I}\\&&\mathbf{I}&\mathbf{B}\end{pmatrix}_{(N-1)}$$

$$\mathbf{B}=\begin{pmatrix}-2&&\\&\ddots&\\&&-2\end{pmatrix}_{(M-1)}$$

$$\mathbf{I}=\begin{pmatrix}1&&\\&\ddots&\\&&1\end{pmatrix}_{(M-1)}.$$

For $\mathbf{C}_l$,

$$\mathbf{C}_l=\begin{pmatrix}\mathbf{P}&&&&&\\&\mathbf{Q}_{67}&&&&\\&&\mathbf{Q}_{68}&&&\\&&&\ddots&&\\&&&&\mathbf{Q}_{283}&\\&&&&&\mathbf{P}\end{pmatrix}_{349\times349=121\,801}$$

where

$$\mathbf{P}=\begin{pmatrix}\mathbf{C}_2&&\\&\ddots&\\&&\mathbf{C}_2\end{pmatrix}_{349\times66=23\,034}$$

$$\mathbf{Q}_j=\begin{pmatrix}\mathbf{D}&&\\&\mathbf{F}&\\&&\mathbf{D}\end{pmatrix}$$

$$\mathbf{D}=\begin{pmatrix}\mathbf{C}_2&&\\&\ddots&\\&&\mathbf{C}_2\end{pmatrix}_{x_1(j)}$$

$$\mathbf{F}=\begin{pmatrix}\mathbf{C}_2 & & \\ & \ddots & \\ & & \mathbf{C}_2\end{pmatrix}_{x_2(j)}$$

with

$$x_1(j)=\left[112.5-(j-67)\tan 30^\circ\right]$$

$$x_2(j)=349-2x_1$$

where $[\cdot]$ means round down to the nearest integer.

Acknowledgment

This work is supported by the National Natural Science Foundation of China (Grant Nos. 62025505 and 62061136002).

Declarations

Conflict of Interest Minghong YANG is an editorial board member for Photonic Sensors and was not involved in the editorial review, or the decision to publish this article. All authors declare that there are no competing interests.

References

[1] H. Jiang, Z. Cao, R. Yang, L. Yuan, H. Xiao, and J. Dong, "Synthesis and characterization of spinel $MgAl_2O_4$ thin film as sapphire optical fiber cladding for high temperature applications," *Thin Solid Films*, 2013, 539: 81–87.

[2] H. Chen, F. Tian, J. Kanka, and H. Du, "A scalable pathway to nanostructured sapphire optical fiber for evanescent-field sensing and beyond," *Applied Physics Letters*, 2015, 106(11): 8–61.

[3] B. Wilson and T. Blue, "Creation of an internal cladding in sapphire optical fiber using the ^{6}Li(n, α)^{3}H reaction," *IEEE Sensors Journal*, 2017, 17(22): 7433–7439.

[4] H. Chen, M. Buric, P. Ohodnicki, J. Nakano, B. Liu, and B. Chorpening, "Review and perspective: Sapphire optical fiber cladding development for harsh environment sensing," *Applied Physics Reviews*, 2018, 5(1): 011102.

[5] J. Wang, B. Dong, E. Lally, J. Gong, M. Han, and A. Wang, "Multiplexed high temperature sensing with sapphire fiber air gap-based extrinsic Fabry-Perot interferometers," *Optics Letters*, 2010, 35(5): 619–621.

[6] Y. Zhu and A. Wang, "Surface-mount sapphire interferometric temperature sensor," *Applied Optics*, 2006, 45(24): 6071–6076.

[7] Y. Zhu, Z. Huang, F. Shen, and A. Wang, "Sapphire-fiber-based white-light interferometric sensor for high temperature measurements," *Optics Letters*, 2005, 30(7): 711–713.

[8] Y. Yao, W. Liang, X. Gui, and F. Dian, "Sapphire Fabry-Perot high-temperature sensor study," in *The 25th Optical Fiber Sensors Conference*, Jeju, Republic of Korea, 2017, pp. 1–4.

[9] J. Yi, "Adhesive-free bonding of monolithic sapphire for pressure sensing in extreme environments," *Sensors*, 2018, 18(8): 2712.

[10] X. Yu, S. Wang, J. Jiang, K. Liu, J. Dong, P. Zhang, *et al.*, "Hybrid sapphire dual-Fabry-Perot-cavities sensor for high temperature and refractive index measurement," *Journal of Lightwave Technology*, 2021, 39(12): 3911–3918.

[11] Y. Cheng, C. Hill, B. Liu, Z. Yu, H. Xuan, D. Homa, *et al.*, "Modal reduction in single crystal sapphire optical fiber," *Optical Engineering*, 2015, 54(10): 107103.

[12] Y. Cheng Y, C. Hill, B. Liu, Z. Yu, H. Xuan, D. Homa, *et al.*, "Design and analysis of large-core single-mode windmill single crystal sapphire optical fiber," *Optical Engineering*, 2016, 55(6): 066101.

[13] C. Hill, D. Homa, B. Liu, Z. Yu, A. Wang, and G. Pickrell, "Submicron diameter single crystal sapphire optical fiber," *Materials Letters*, 2015, 138: 71–73.

[14] C. Hill, D. Homa, Z. Yu, Y. Cheng, B. Liu, A. Wang, *et al.*, "Single mode air-clad single crystal sapphire optical fiber," *Applied Sciences*, 2017, 7(5): 473.

[15] X. Feng, Y. Jiang, S. Xie, Y. Cui, and Y. Zhang, "Higher-order mode suppression technique for multimode sapphire fiber external Fabry-Perot interferometers," *Optics Express*, 2022, 30(4): 4759–4767.

[16] J. Zhang, D. Zhang, C. Pan, and M. Yang, "Sapphire fiber Fabry-Perot sensors with high fringe visibility," *IEEE Photonics Journal*, 2022, 14(4): 1–8.

[17] F. Pérennès, P. Beard, and T. Mills, "Analysis of a low-finesse Fabry-Perot sensing interferometer illuminated by a multimode optical fiber," *Applied Optics*, 1999, 38(34): 7026–7034.

[18] M. Han and A. Wang, "Exact analysis of low-finesse multimode fiber extrinsic Fabry-Perot interferometers," *Applied Optics*, 2004, 43(24): 4659–4666.

[19] M. Han and A. Wang, "Mode power distribution effect in white-light multimode fiber extrinsic Fabry-Perot interferometric sensor systems," *Optics Letters*, 2006, 31(9): 1202–1204.
[20] W. Dai, X. Sun, and M. Zhang, "Research on offset launch of POF and light source," *SPIE International Symposium on Optoelectronics and Microelectronics*, *Fiber Optic Components, Subsystems, & Systems for Telecommunications*, 2001, 4604:135–143.
[21] F. Mumtaz, M. Ashraf, Y. Dai, and W. Hu, "Numerical solution of strongly guided modes propagating in sapphire crystal fibers (α-Al_2O_3) for UV, VIS/IR wave-guiding," *Results in Physics*, 2020, 18: 103311.
[22] B. Saleh and M. Teich, "*Fundamentals of Photonics*," New Jersey: Wiley, 2019.
[23] D. Marcuse, "*Theory of Dielectric Optical Waveguides*," Salt Lake City: Academic Press, 1974.
[24] Z. Li, Z. Qiao, and T. Tang, "*Numerical solution of differential equations: introduction to finite difference and finite element methods*," Cambridge: Cambridge University Press, 2017.